

**Transport properties of antimony nanowires**

J. Heremans and C. M. Thrush

*Delphi Research Labs, Delphi Automotive Systems, Shelby Township, Michigan 48316*

Yu-Ming Lin

*Department of Electrical Engineering and Computer Science, Massachusetts Institute of Technology, Cambridge, Massachusetts 02139*

S. B. Cronin

*Department of Physics, Massachusetts Institute of Technology, Cambridge, Massachusetts 02139*

M. S. Dresselhaus\*

*Department of Physics and Department of Electrical Engineering and Computer Science, Massachusetts Institute of Technology, Cambridge, Massachusetts 02139*

(Received 14 June 2000; revised manuscript received 27 September 2000; published 1 February 2001)

This paper reports the temperature dependence of the resistivity and the longitudinal and transverse magnetoresistance of antimony quantum wires with diameters ranging from 200 down to 10 nm. The samples were prepared in porous anodic alumina host materials using the vapor-phase technique. A theoretical calculation of the band structure of Sb nanowires is presented and a transport model for nanowire systems is used to explain the measured temperature dependence of the resistivity, showing both classical and quantum finite-size effects. The magnetoresistance is quadratic at low fields. In the 200 nm wires, the low-temperature ( $T < 50$  K) longitudinal magnetoresistance exhibits a maximum at the magnetic field where the cyclotron radius roughly corresponds to the wire radius. Surface scattering dominates below that field, and bulklike scattering dominates above it. In the narrower wires, the low-temperature (below 10 K for 50 nm wires and below 40 K for 10 nm wires) magnetoresistance shows a steplike feature at the critical magnetic field where the magnetic length equals the wire diameter, as was the case for bismuth wires. This phenomenon is independent of the effective masses, depending only on the geometry of the nanowires and on the magnetic flux in the wire, and it is therefore attributed to a localization effect.

DOI: 10.1103/PhysRevB.63.085406

PACS number(s): 73.40.-c

**INTRODUCTION**

The transport properties of bismuth (Bi) thin wires have been investigated extensively for several decades.<sup>1-3</sup> A second wave of studies has been more recently initiated as a result of the calculations of Hicks and Dresselhaus,<sup>4</sup> who predicted that Bi nanowires should have a thermoelectric figure of merit strongly enhanced over that for bulk Bi, and possibly higher than for conventional thermoelectric materials. Zhang *et al.*<sup>5</sup> synthesized Bi nanowires in porous anodic alumina using a high-pressure liquid injection technique, similar to that in the older work, but using a surfactant to lower the pressure necessary for filling the pores. A vapor-phase preparation technique<sup>6</sup> was developed to prepare Bi nanowires with diameters down to 7 nm. Both preparation techniques produce Bi nanowires with a preferential crystallographic orientation: the long axis of the wires aligns with the  $[10\bar{1}1]$  or  $[01\bar{1}2]$  directions in the hexagonal structural description (or  $[x,y,z]=[0,0.949,0.315]$  and  $[0,0.834,0.552]$  in Cartesian coordinates, respectively).<sup>3,5,6</sup> Exceptions to these two orientations are the Bi wires of Huber *et al.*,<sup>7</sup> which are reported to have a long axis along the trigonal  $[0001]$  direction, and the Bi wires prepared by electrochemical means,<sup>8</sup> which are polycrystalline. The galvanomagnetic,<sup>6,9,10</sup> thermoelectric,<sup>11,12</sup> and thermal<sup>13</sup> properties of the  $[10\bar{1}1]$ -oriented Bi nanowire arrays have been extensively reported.

In the present paper, we extend this work to nanowire

arrays of another group-V semimetal: antimony (Sb). As in Bi, electronic transport phenomena in Sb occur via both electrons and holes. The energy overlap between the conduction and valence bands is about 180 meV at 4.2 K.<sup>14,15</sup> The electrons are located, as in Bi, in three ellipsoidal carrier pockets centered at the  $L$  points of the Brillouin zone. Each electron Fermi ellipsoid<sup>14</sup> has a long axis tilting by about  $-4^\circ$  from the bisectrix axis. The effective-mass components of the electron ellipsoids in Sb are much larger than those in Bi. The hole Fermi surface of Sb is quite complex, but can be approximated by two sets of three prolate ellipsoids at the equivalent  $H$  points of the Brillouin zone,<sup>15</sup> with the principal axes of the three ellipsoids in each set pointing to a  $T$  point of the Brillouin zone. The longest and shortest axes of the hole ellipsoids are in the trigonal-bisectrix plane, with the intermediate axis oriented along the binary axis. The angle between their longest axis and the trigonal axis is about  $53^\circ$ . The effective-mass components of the hole ellipsoids of Sb are of the same order of magnitude as those in Bi.

The Sb wire arrays were prepared in porous anodic alumina templates using the vapor-phase deposition technique,<sup>6</sup> similar to those used for our previous Bi work. Here we report the temperature dependence of the resistance, and the magnetic-field dependence of the longitudinal and transverse magnetoresistance. A theoretical calculation of the band structure of Sb nanowires is presented, using a model for anisotropic carriers confined to an infinite cylindrical wire.<sup>16</sup> A semiclassical transport model for nanowire systems<sup>10</sup> is

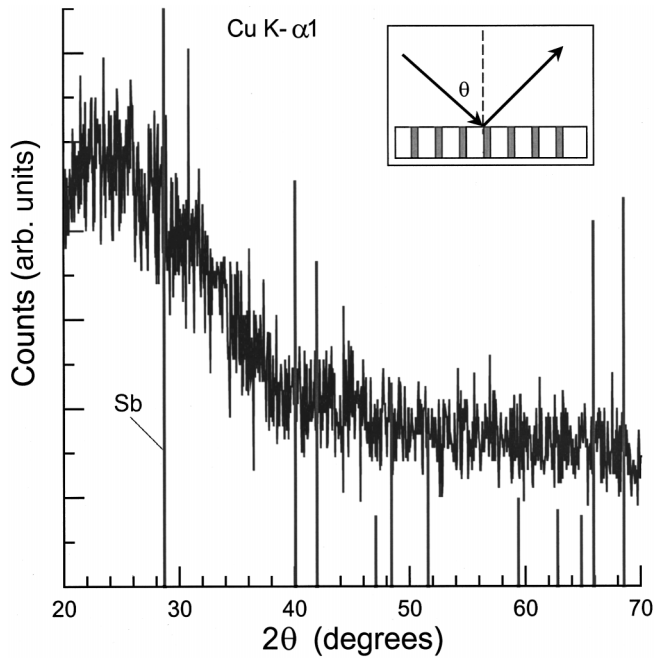


FIG. 1. X-ray diffraction signal vs scattering angle  $2\theta$  of the 200 nm diameter Sb wire array. The vertical lines are the reported peak positions for polycrystalline Sb. The inset shows the sample geometry.

used to explain the measured temperature-dependent resistance for Sb nanowire arrays. The experimental data for the magnetoresistance measurements are interpreted qualitatively by analogy with those for Bi nanowire arrays.

### SAMPLE PREPARATION AND EXPERIMENT

Porous anodic alumina templates<sup>6</sup> were used as host materials for the fabrication of Sb nanowire arrays. Briefly, porous alumina was produced by anodizing pure aluminum films in 20 wt % sulfuric acid, resulting in an array of hexagonally packed pores. Prior to the vapor deposition, the residual aluminum film and the barrier layer are etched away by 0.2M  $\text{HgCl}_2$  and 5 wt %  $\text{H}_3\text{PO}_4$ , respectively, leaving a free-standing alumina template with pores that are open on both sides. The removal of the barrier layer is essential for the following vapor deposition of Sb nanowires and subsequent transport measurements. The pore diameters of the samples used in this work are  $d_w=200$ ,  $48\pm 6$ , and  $10\pm 2$  nm, with an average interpore distance of 400,  $116\pm 6$ , and 50 nm, respectively. The pores were filled with Sb using the same vapor-phase filling apparatus as described in Ref. 6, but with a higher operating temperature. No special care was used during the sample cool-down. An x-ray diffraction spectrum of the 200 nm wire sample is shown in Fig. 1, along with the diffraction peaks for a polycrystalline Sb standard. The inset shows the schematic diagram of the sample setup. Since no peaks are observed in our sample, we conclude that the Sb nanowires are either amorphous or consist of a very fine-grained polycrystalline material.

The resistance and magnetoresistance data were taken on arrays of Sb nanowires using a two-contact technique,<sup>9</sup> with

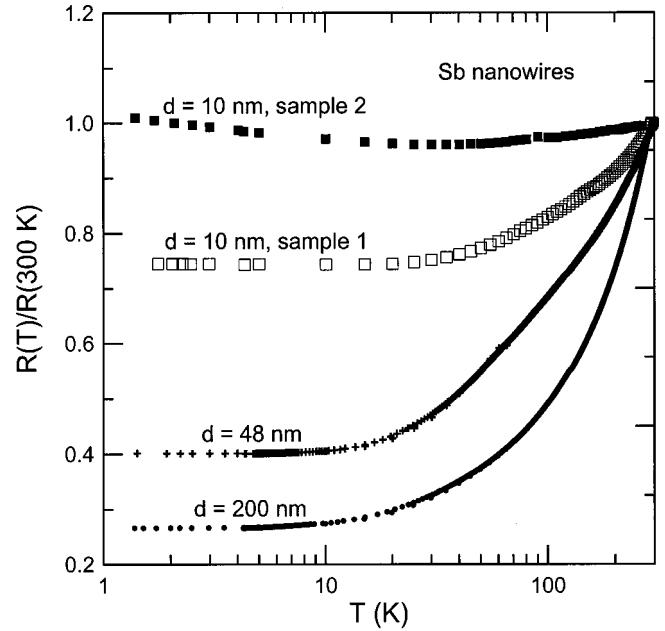


FIG. 2. Experimental temperature dependence of the resistance of Sb nanowires of various diameters, normalized to the resistance at 300 K.

electrical current flowing parallel to the wire axis. The discussion on contact resistance issues reported in Refs. 6 and 9 also holds here. In particular, two samples of each diameter were measured and the results were found to be reproducible, unless otherwise indicated. The samples were placed inside a variable-temperature inset in a 5 T superconducting magnet, and the resistances were measured by a low-frequency ac impedance bridge (Linear Instruments LR-700). The results are independent of excitation voltage, which was varied from 2 to 600  $\mu\text{V}$ . Resistance data were taken from 1.4 to 300 K, while results of the magnetoresistance are reported only from 1.4 to 70 K because the magnet cannot be activated above 80 K. Both the longitudinal magnetoresistance (magnetic field  $B$  parallel to current) and the transverse magnetoresistance ( $B$  normal to current) were measured.

### ZERO-FIELD TEMPERATURE-DEPENDENT RESISTANCE

#### Experimental results

Figure 2 shows the temperature dependence of the resistance of the Sb nanowires, normalized to the resistance at 300 K, in the absence of a magnetic field. The results for the larger-diameter wires are reproducible from sample to sample. One sample of the 10 nm wire shows less temperature variation than the other, probably due to a different distribution in wire diameter or in impurity content. The  $R(T)$  of Sb nanowires exhibits a rather different trend from those for Bi nanowires as the wire diameter varies. Contrasting Fig. 2 with Fig. 3 of Ref. 6, one notices that the clear signature of the semimetal-to-semiconductor transition observed in Bi nanowires<sup>6</sup> is absent in Sb nanowires for the measured diameter range. For Bi nanowires with diameters  $d_w$  ranging

TABLE I. Calculated subband structure parameters for Sb nanowires oriented along the three major axes. The parameters  $\tilde{\varepsilon}_h$  and  $\tilde{\varepsilon}_e$  (in units of meV nm<sup>2</sup>) and  $\tilde{m}_e^*$  (in units of the free-electron mass) can be used in Eqs. (3) and (4) to derive the first-subband-edge energies and the transport effective masses of the charge carriers. The hole transport mass  $m_h^*$  is also given in units of the free-electron mass.

Orientation	Trigonal	Bisectrix		Binary	
		Group I	Group II	Group I	Group II
$\tilde{\varepsilon}_h$	$9.70 \times 10^3$	$1.25 \times 10^4$	$9.88 \times 10^3$	$8.78 \times 10^3$	$1.17 \times 10^4$
$m_h^*$	0.340	0.630	0.209	0.068	0.490
$\tilde{\varepsilon}_e$	$1.08 \times 10^4$	$2.13 \times 10^4$	$1.41 \times 10^4$	$1.14 \times 10^4$	$1.89 \times 10^4$
$\tilde{m}_e^*$	0.043	0.525	0.163	0.043	0.404

from 10 to 200 nm, the measured resistance changes from a monotonic  $T$  dependence to a nonmonotonic dependence as  $d_w$  increases, while  $R(T)$  of Sb nanowire arrays in this range of  $d_w$  exhibits less variation in  $T$ . Qualitatively, the gross features of Fig. 2 can be explained in terms of the relative importance of electron-phonon scattering, which increases with temperature, and electron-boundary scattering, which is relatively  $T$  independent. Since the Sb nanowires are expected to remain metallic for the measured diameter range (as will be shown later), the carrier density is a weak function of  $T$ , and the  $R(T)$  is mainly determined by the  $T$  dependence of the various scattering mechanisms. At high temperatures ( $T > 100$  K), the phonon scattering dominates and the resistance rises with increasing  $T$ . As the temperature is lowered, the boundary scattering becomes dominant, giving rise to a less  $T$ -dependent resistance for  $T < 100$  K, which explains the general features of the measure  $R(T)$  for the various Sb nanowire arrays shown in Fig. 2. As the wire diameter decreases, the boundary scattering becomes relatively more important than for larger-diameter wires, since a larger portion of the carriers are located near the wire boundary. Therefore, smaller-diameter wires exhibit less temperature variation than larger-diameter wires.

### Theoretical modeling

In order to quantitatively explain the experimental results in Fig. 2, a semiclassical transport model for the Sb nanowires is developed, based on the detailed band structure of Sb nanowires. The band structure of Sb nanowires is derived from a model developed recently for Bi nanowire systems to determine the subband structure of anisotropic carriers confined within a cylindrical wire of infinite length.<sup>16</sup> In addition, due to the coupling between the holes and electrons at the  $L$  points of the Brillouin zone of Sb, the following nonparabolic dispersion relation is used for the  $L$ -point carriers:<sup>14</sup>

$$E_L(\mathbf{k}) = -\frac{E_g}{2} \pm \sqrt{E_g^2 + 2E_g \hbar^2 \mathbf{k} \cdot \vec{\alpha} \cdot \mathbf{k}}, \quad (1)$$

where  $E_g \approx 100$  meV is the direct band gap at the  $L$  point<sup>17</sup> and  $\vec{\alpha}$  is the inverse effective-mass tensor at the band edge. The subbands formed by carriers confined in an infinite cylindrical quantum wire, with the wire axis denoted by the  $z$  direction, have an  $E(k)$  dispersion relation of the form<sup>16</sup>

$$E_{nm}(k_z) = \varepsilon_{nm} + \frac{\hbar^2 k_z^2}{2m_z^*}, \quad (2)$$

where  $\varepsilon_{nm}$  is the band-edge energy of the  $(n, m)$  subband calculated to include nonparabolic effects, and  $m_z^* = \hat{z} \cdot \vec{\alpha}^{-1} \cdot \hat{z}$  is the transport effective mass along the wire axis.<sup>16</sup> Since the dispersion energy is small, a parabolic approximation is sufficient to describe the  $k_z$  dependence. Using the band structure parameters of bulk Sb, the energy shifts of the first subband edges of each electron and hole pocket with respect to the corresponding band edges in bulk Sb are given by<sup>16</sup>

$DE(d_w)$

$$= \begin{cases} -\tilde{\varepsilon}_h/d_w^2 & \text{(meV) for holes} \\ -E_g + \sqrt{E_g^2 + 4\tilde{\varepsilon}_e E_g/d_w^2} & \text{(meV) for electrons,} \end{cases} \quad (3)$$

where  $d_w$  is the wire diameter in nanometers, and  $\tilde{\varepsilon}_e$  and  $\tilde{\varepsilon}_h$  are parameters calculated numerically using the cylindrical boundary conditions. It is noted that due to the anisotropic carriers in Sb the subband-edge energies  $\varepsilon_{nm}$  and the transport effective mass  $m_z^*$  are both highly dependent on the wire orientation. Values for the calculated  $\tilde{\varepsilon}_e$ ,  $\tilde{\varepsilon}_h$ , and transport effective masses  $m_z^*$  are given in Table I for Sb nanowires oriented along the three major axes. As in Bi, the transport effective mass  $m_z^*$  of the  $L$ -point carriers in Sb is a function of the subband-edge energy  $\varepsilon_{nm}$  due to the nonparabolicity.<sup>16</sup> The effective masses of these nonparabolic carriers are then determined by the curvature of the dispersion relation at the subband edge, which is given by<sup>16</sup>

$$m_z^* = \sqrt{1 + 4\tilde{\varepsilon}_{nm}/E_g} \cdot \tilde{m}_z^*, \quad (4)$$

where  $\tilde{m}_z^*$  are the values given in Table I. We note that, for trigonal Sb wires, the three electron pockets and the six hole pockets are degenerate. However, for wires oriented along the binary and bisectrix directions, the carrier pockets are divided into two groups, based on symmetry considerations. The carrier pockets with their major axes lying in the plane spanned by the wire axis and the trigonal axis for bisectrix wires or in the plane perpendicular to the wire axis for binary wires are denoted as group I, while other pockets that possess different symmetries are denoted as group II. Therefore,

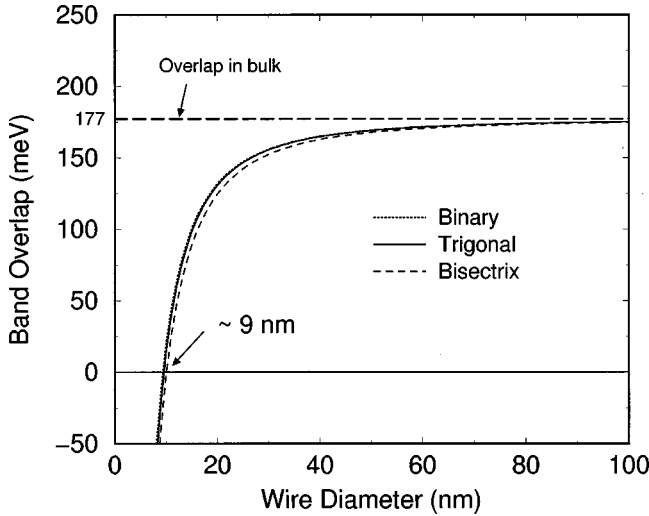


FIG. 3. Calculated band overlap between the electrons and holes as a function of wire diameter for the three major crystalline orientations of the Sb nanowires. The critical wire diameters at which the band overlap vanishes are about 9 nm.

for binary and bisectrix wires, the two groups of pockets form two sets of subbands with different transport effective masses along the wire axis (see Table I).

Due to quantum confinement effects, the subband edges of the electrons and holes shift in opposite directions, decreasing the band overlap between the  $L$ -point conduction and the  $H$ -point valence bands. As  $d_w$  continues to decrease, the band overlap will eventually vanish, leading to a semimetal-semiconductor transition in Sb nanowires. Figure 3 shows the calculated band overlap for Sb nanowires as a function of  $d_w$  for the three major crystalline orientations along the nanowire axis. The critical wire diameters  $d_c$  for the semimetal-semiconductor transition at which the band overlap is predicted to vanish are 9.6, 10.0, and 9.3 nm for Sb wire axes oriented along the trigonal, bisectrix, and binary directions, respectively. These calculation show that the critical wire diameters  $d_c$  are much smaller than those of Bi nanowires, which are predicted to be between 40 and 55 nm at 77 K,<sup>16</sup> depending on the wire orientation. These smaller values for the critical wire diameter are consistent with the much larger band overlap and higher carrier effective masses of Sb relative to Bi.

Since the samples used here did not show any preferred crystallographic orientation (see Fig. 1) and the band parameters of Sb wires are not very different from each other for wires oriented along the three major orientations (see Fig. 3), we choose the trigonal wire orientation, as an example, for the following transport modeling. Figure 4 shows the calculated total carrier density in Sb nanowires for various wire diameters. We note that the carrier densities in Sb nanowires are lower than those of bulk Sb and the carrier densities decrease as  $d_w$  decreases, because of a smaller band overlap for narrower wires. However, the temperature dependence of the carrier density for Sb wires did not change significantly as the wire diameter was varied down to 10 nm, in contrast to that of Bi nanowires, which shows a strong diameter dependence in this diameter range.<sup>16</sup> This different behavior is

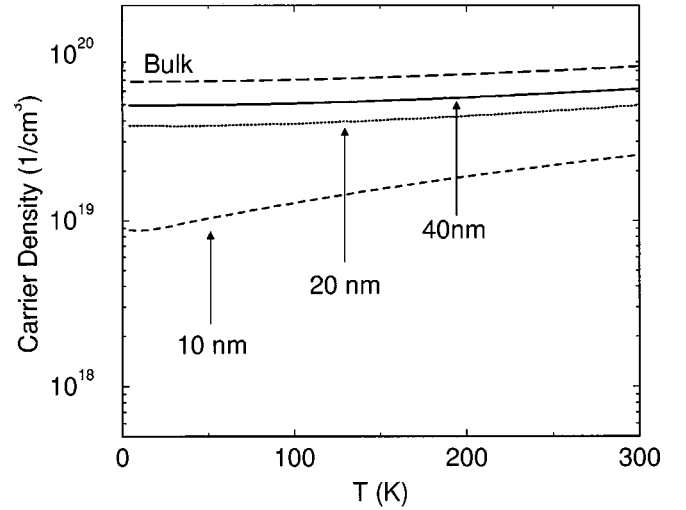


FIG. 4. Calculated total carrier density as a function of temperature for Sb nanowires with various diameters, compared to that of bulk antimony.

due to a less  $T$ -dependent band structure and a much larger band overlap in bulk Sb as compared to Bi. The carrier density of 10 nm Sb wires exhibits a slightly stronger  $T$  dependence than other larger-diameter wires in Fig. 4, since 10 nm is close to the critical wire diameter for the semimetal-semiconductor transition. Figure 5 shows the calculated  $R(T)$  for 10 and 48 nm trigonal Sb nanowire arrays, displaying trends qualitatively consistent with the experimental results shown in Fig. 2. In the semiclassical transport model, the conductivity of the one-dimensional (1D) systems is derived by<sup>16</sup>

$$\sigma = \sum_i^{\text{pockets}} \sum_{n,m}^{\text{subbands}} \frac{4e\mu_i m_{(i,n,m)}^*}{\pi^2 d_w^2} \int dk \left( -\frac{df}{dE} \right) v(k)v(k), \quad (5)$$

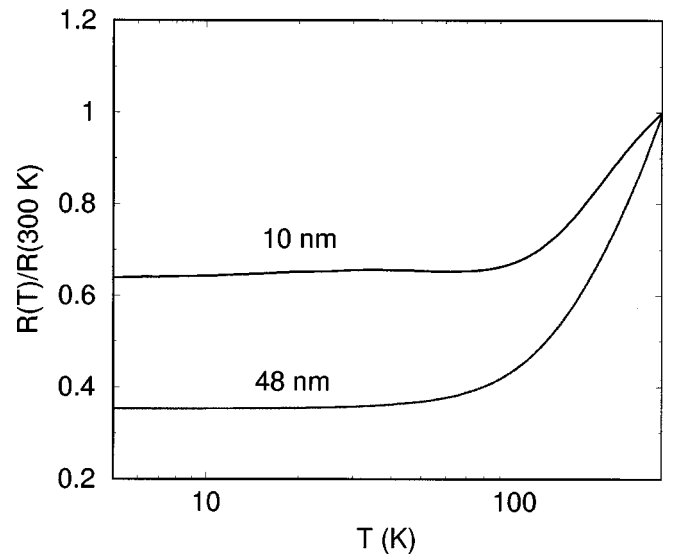


FIG. 5. Calculated temperature dependence of the resistance for 48 and 10 nm Sb nanowires, normalized to the resistance at 300 K.

where  $m_{(i,n,m)}^*$  is the transport effective mass of the  $(n,m)$  subband in the  $i$ th pocket,  $\mu_i$  is the carrier mobility,  $v$  is the carrier group velocity, and  $f(E)$  is the Fermi-Dirac distribution function. In addition to the dominant electron-phonon scattering in bulk Sb, the expected carrier scattering at the wire boundary and at grain boundaries in nanowires is taken into consideration by Matthiesen's rule:<sup>18</sup>

$$\mu_{\text{tot},i}^{-1} = \mu_{\text{bulk},i}^{-1} + \mu_{\text{bound}}^{-1}, \quad (6)$$

where  $\mu_{\text{bulk},i}$  is the carrier mobility of the  $i$ th pocket along the wire axis in bulk crystalline Sb, and  $\mu_{\text{bound}}^{-1}$  is the contribution to the total scattering rate from boundary scattering. Since the mobility of each carrier pocket in Sb is anisotropic, we have  $\mu_{\text{bulk},i}^{-1} = \hat{z} \cdot \vec{\mu}_i^{-1} \cdot \hat{z}$ , where  $\vec{\mu}_i$  is the mobility tensor of the  $i$ th carrier pocket. The mobility tensor components of  $\vec{\mu}_i$  are highly temperature dependent, and empirical relations from the literature<sup>19</sup> for single-crystal Sb are used here. On the other hand, the band structure parameters of Sb, unlike Bi, are relatively temperature independent<sup>20</sup> for  $4 < T < 300$  K, and are assumed to be constant in the calculations. The curve of  $R(T)$  normalized to the room-temperature resistance for the 10-nm Sb nanowire arrays in Fig. 5 is fitted by  $\mu_{\text{bound}} = 6.67 \times 10^{-2} \text{ m}^2/\text{V s}$  and the carrier density contribution due to the uncontrolled impurities is fitted by  $N_{\text{imp}} = 4 \times 10^{18} \text{ cm}^{-3}$ . The data for the 48-nm Sb nanowires are fitted by  $\mu_{\text{bound}} = 1.0 \times 10^{-1} \text{ m}^2/\text{V s}$ . Since 48-nm Sb nanowires are still semimetallic with a large band overlap ( $\sim 168 \text{ meV}$ ), the carrier density contribution due to  $N_{\text{imp}}$  can be neglected. We note that the  $\mu_{\text{bound}}$  calculated here is about two orders of magnitude smaller than for the case of highly crystalline Bi nanowires ( $\mu_{\text{bound}} = 33 \text{ m}^2/\text{V s}$  for 36-nm Bi nanowire arrays).<sup>10</sup> Since the Sb nanowires used here are polycrystalline with many grain boundaries,  $\mu_{\text{bound}}$  is expected to be more dominant and to have a lower value than in single-crystal wires. In addition, the larger carrier effective masses in Sb may also contribute to the lower value of  $\mu_{\text{bound}}$ . The fact that the measured  $R(T)$  of Sb and Bi nanowires can be explained by the same transport model suggests that the different temperature dependence of the resistance in nanowires from that of the bulk materials is a consequence of both quantum and classical finite-size effects. The classical finite-size effect decreases the carrier mobility by limiting the carrier mean free path, while the quantum confinement effect alters the band structure, especially for semimetals, and changes the carrier density significantly. The two factors together determine the temperature dependence of the resistance in the nanowire system.

### MAGNETORESISTANCE

The measured longitudinal and transverse magnetoresistance of the 200, 48, and 10 nm Sb nanowires as a function of magnetic field  $B$  are shown in Figs. 6, 7, and 8, respectively. The magnetic-field dependence of the resistance at each temperature is normalized to the resistance at zero field at the same temperature. Note that the amplitude of the normalized magnetoresistance is two orders of magnitude smaller in the 10 nm wires than in the 200 nm wires, so that

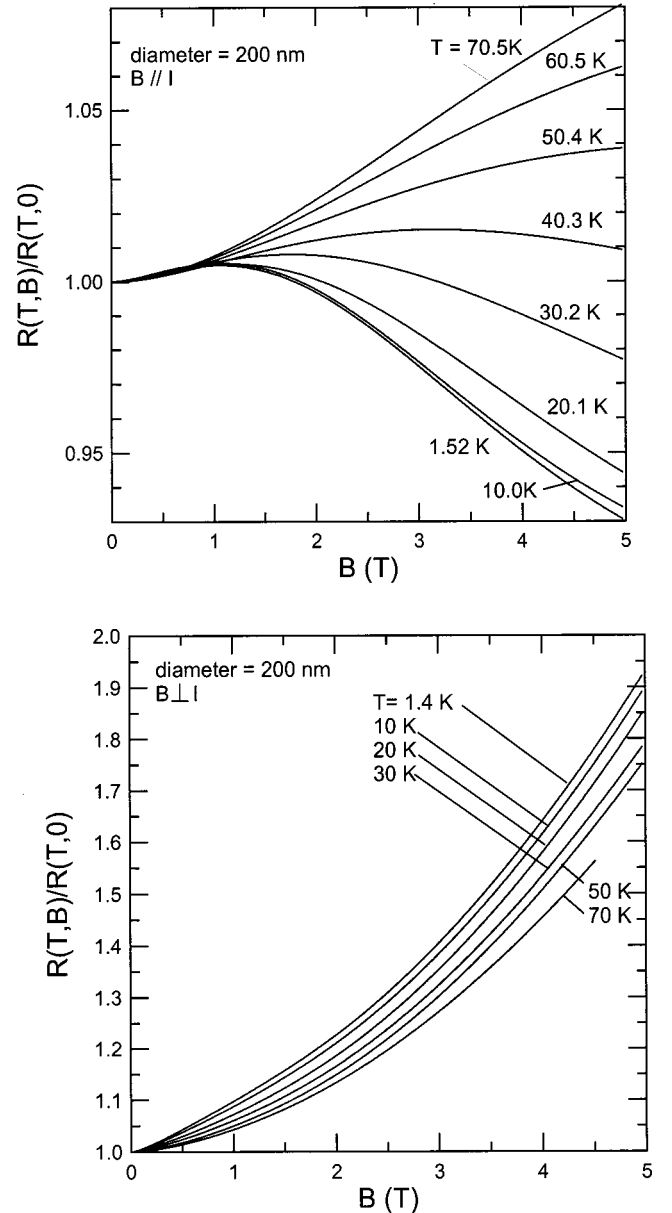


FIG. 6. Experimental longitudinal ( $B \parallel I$ ) and transverse ( $B \perp I$ ) magnetoresistance of 200 nm Sb nanowires, as a function of magnetic field, for the various temperatures indicated. The resistance at each field is normalized to the resistance at zero field at the same temperature.

the measurement noise is much more visible in Fig. 8.

At low magnetic fields, the magnetoresistance of most samples can be described by a parabolic relation:

$$R(B,T)/R(0,T) - 1 = AB^2, \quad (7)$$

where  $A$  is the magnetoresistance coefficient. In a multicarrier system with anisotropic Fermi surfaces,  $A$  is essentially related to the mobility tensor elements.<sup>21</sup> The temperature dependence of  $A$  is shown in Fig. 9. The 200 and 48 nm Sb nanowires show essentially a monotonic decrease of  $A$  with increasing  $T$  (with the exception of a few data points in the longitudinal magnetoresistance of the 200 nm sample above

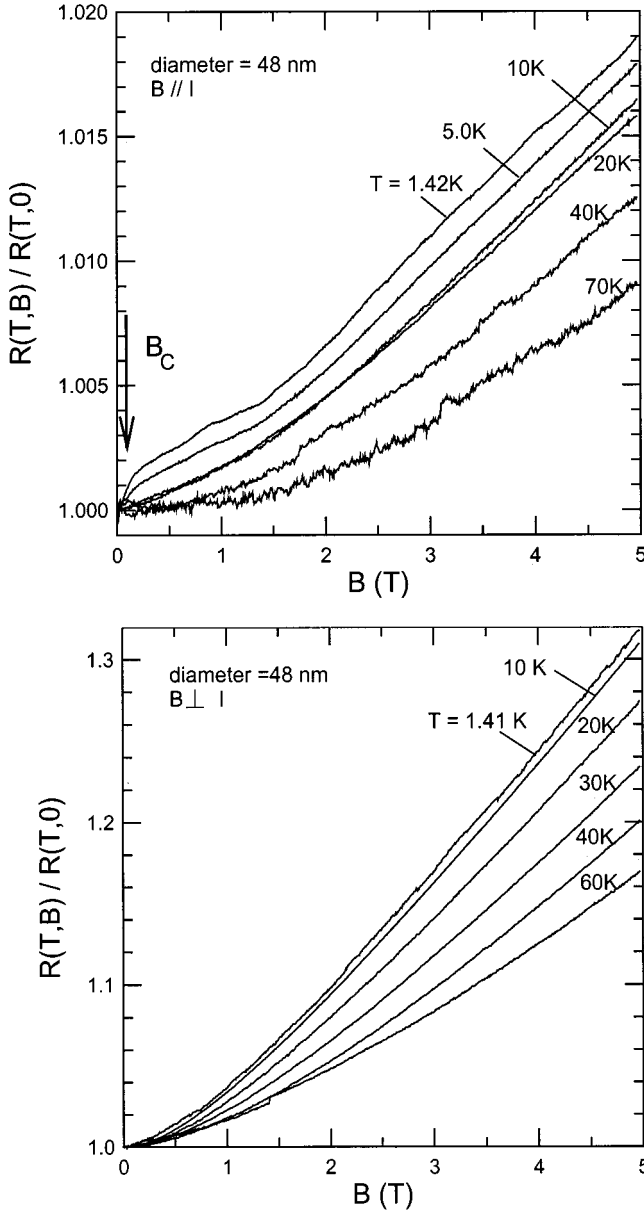


FIG. 7. Magnetic-field dependence of the longitudinal ( $B\parallel I$ ) and transverse ( $B\perp I$ ) magnetoresistance of the 48 nm Sb nanowires, as in Fig. 6.

50 K), consistent with a substantial contribution of phonon scattering to the total mobility  $\mu_{\text{tot}}$ . The case of 10-nm Sb wires is discussed later in this text.

#### 200 nm diameter wires

It is noted that the low-temperature (1.4–10 K) longitudinal magnetoresistance of the 200 nm Sb wires has a maximum at  $B \approx 1.2$  T (see Fig. 3). As in the case of semimetallic Bi nanowires, we attribute this maximum to the condition where the cyclotron radius  $R_c$  equals the wire radius, which is consistent with the theory of Chambers.<sup>22</sup> The cyclotron radius  $R_c$  is given by

$$R_c = \frac{v_F}{\omega_c} = \frac{\hbar k_{zF}}{eB_z}, \quad (8)$$

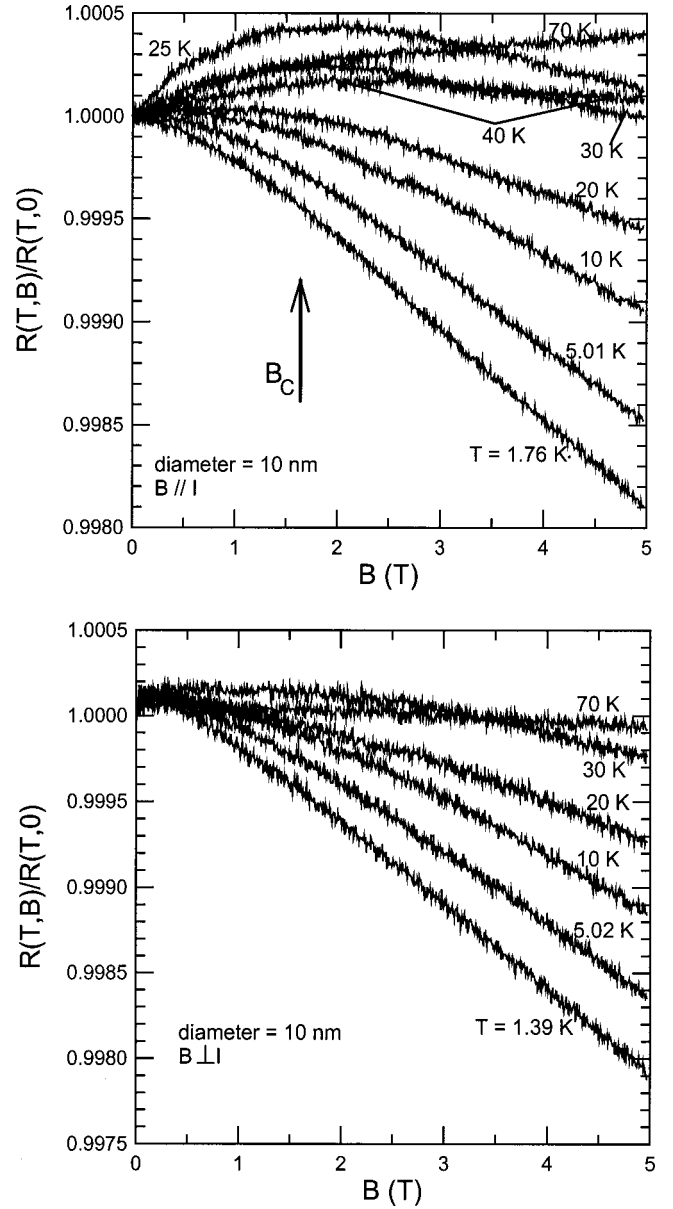


FIG. 8. Magnetic-field dependence of the longitudinal ( $B\parallel I$ ) and transverse ( $B\perp I$ ) magnetoresistance of the 10 nm Sb nanowires, sample 1 in Fig. 2.

where  $v_z$  is the carrier group velocity along the wire axis direction  $z$ ,  $\omega_c$  is the cyclotron frequency,  $B_z$  is the longitudinal magnetic field, and  $k_{zF}$  is the carrier Fermi wave vector along the  $z$  axis. When the magnetic field is lower than the critical field at which the cyclotron orbit can fit within a nanowire, the transport phenomena are dominated by the scattering at the wire surfaces. The mobility is then relatively low; the resistance increases with  $B$  since the magnetic field deflects the carrier trajectories and increases the scattering at the wire boundary. At high fields where  $2R_c < d_w$ , the transport phenomena become closer to those in bulk Sb. In this high-field regime, the mobility is limited less by the wire surface than by phonon and grain-boundary scattering mechanisms. Thus, at fields  $B > B_{\text{cy}}$ , where  $2R_c(B_{\text{cy}}) = d_w$ , the wire resistance starts decreasing because the ra-

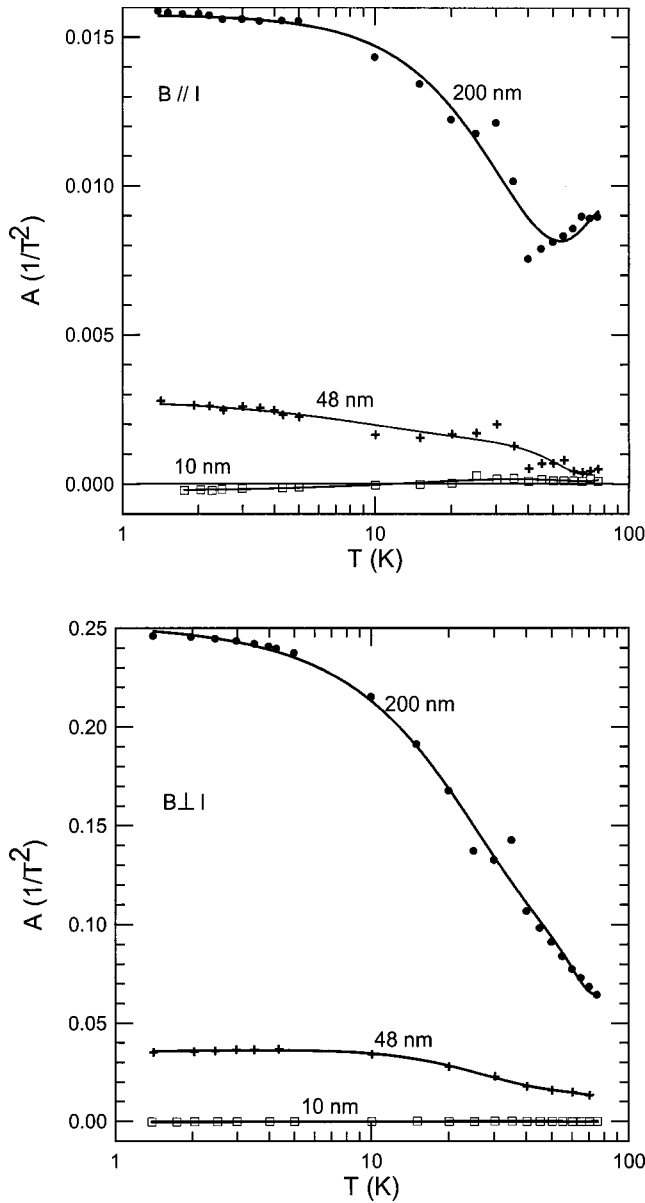


FIG. 9. Experimental temperature dependence of the longitudinal ( $B\parallel I$ ) and transverse ( $B\perp I$ ) magnetoresistance coefficients  $A$  of the Sb nanowires with the diameters indicated.

dius of the carrier trajectory is smaller than the wire radius, causing a decrease in the boundary scattering. Assuming Sb wires with the long axis oriented along the trigonal direction, the calculated  $B_{cy}$  is 3.0 and 2.2 T for electrons and holes, respectively. This is the field range in which the maximum in the longitudinal magnetoresistance is observed in Fig. 6 ( $B\parallel I$ ). However, it should be noted that the observed field strength for the resistance maximum depends on the relative intensity of the phonon scattering, grain-boundary scattering, and surface scattering, and therefore is temperature dependent and somewhat sample dependent.

#### Narrower wires

In contrast to the transport properties that depend on the band structure, the features that were ascribed to the local-

ization effect<sup>9</sup> in Bi nanowires are also present in the Sb nanowires at the same values of the magnetic field. For example, the magnetic field  $B_c$  at which the magnetic length [Eq. (10) in Ref. 23]  $L_H$  equals the wire diameter  $d_w$  is indicated as an arrow in Figs. 7 and 8:

$$L_H(B_c) = \sqrt{\frac{\hbar}{4eB_c}} = d_w. \quad (9)$$

As was the case for Bi nanowires,<sup>9</sup> a steplike increase in the longitudinal magnetoresistance of the 48-nm wires is readily observed at  $B_c$  at 1.4 K (see Fig. 7), which becomes weaker at 5 K and is absent for  $T > 10$  K. The same feature is weakly visible in the transverse magnetoresistance but it is masked by the much larger quadratic background. The 10 nm Sb wires exhibit a somewhat different behavior:  $R(B)$  has a maximum located near  $B_c$  for  $T \approx 25$ –30 K. Below 20 K, the resistance decreases monotonically with increasing magnetic field and increases monotonically above 40 K. In analogy to previous studies on Bi nanowires,<sup>9</sup> we suggest that the steplike behavior in Fig. 7 and the maximum in Fig. 8 are related to the transition from a 1D localization system at low magnetic fields to a 3D localization system at high fields. As suggested by Beutler and Giordano,<sup>23</sup> the system becomes essentially three dimensional when  $L_H < d_w$ , while at low magnetic fields 1D localization dominates.

#### SUMMARY

In summary, antimony nanowires were prepared with diameters down to 10 nm in porous anodic alumina by the vapor-phase technique. In contrast to the case of Bi nanowires, the Sb nanowires are fine-grained polycrystals or amorphous. They remain metallic as the diameter is decreased down to 10 nm, and do not exhibit the semimetal-to-semiconductor transition that has been observed in Bi nanowires. This is consistent with the calculated band structure for Sb nanowires, which predicts the transition to occur below 10 nm due to the much larger values of the electron effective masses and larger band overlap between the electrons and holes in Sb. A semiclassical transport model for nanowires gives calculated zero-field  $R(T)$  results that are consistent with the experimental measurements, showing that both quantum and classical confinement effects play important roles in determining the temperature dependence of the resistance in Sb nanowires. From magnetoresistance measurements, it appears that the localization effects that are already observed in Bi nanowires are similarly present in Sb nanowires, consistent with a definition of the magnetic length that is independent of band structure parameters.

#### ACKNOWLEDGMENTS

The authors thank Dr. G. Dresselhaus for valuable discussions. Support from MURI Subcontract No. 0205-G-7A114-01, NSF Grant No. DMR-98-04734, and U.S. Navy Contract No. N00167-92-K005 is gratefully acknowledged by the MIT authors.

- \*On leave from Department of Physics and Department of Electrical Engineering and Computer Science, Massachusetts Institute of Technology, Cambridge, MA 02139.
- <sup>1</sup>D. A. Glocker and M. J. Skove, *Phys. Rev. B* **15**, 608 (1977).
- <sup>2</sup>N. B. Brandt, D. V. Gitsu, A. A. Nikolaeva, and Ya. G. Ponomarev, *Zh. Eksp. Teor. Fiz.* **72**, 2332 (1977) [*Sov. Phys. JETP* **45**, 1226 (1977)].
- <sup>3</sup>N. B. Brandt, D. V. Gitsu, V. A. Dolma, and Ya. G. Ponomarev, *Zh. Eksp. Teor. Fiz.* **92**, 913 (1987) [*Sov. Phys. JETP* **65**, 515 (1987)].
- <sup>4</sup>L. D. Hicks and M. S. Dresselhaus, *Phys. Rev. B* **47**, 16 631 (1993).
- <sup>5</sup>Z. Zhang, X. Sun, M. S. Dresselhaus, J. Y. Ying, and J. P. Heremans, *Appl. Phys. Lett.* **73**, 1589 (1998).
- <sup>6</sup>J. Heremans, C. M. Thrush, Y. M. Lin, S. Cronin, Z. Zhang, M. S. Dresselhaus, and J. F. Mansfield, *Phys. Rev. B* **61**, 2921 (2000).
- <sup>7</sup>T. E. Huber, M. J. Graf, C. A. Foss, Jr., and P. Constant, *J. Mater. Res.* **15**, 1816 (2000).
- <sup>8</sup>K. Liu, C. L. Chien, and P. C. Searson, *Phys. Rev. B* **58**, R14 681 (1998).
- <sup>9</sup>J. Heremans, C. M. Thrush, Z. Zhang, X. Sun, M. S. Dresselhaus, J. Y. Ying, and D. T. Morelli, *Phys. Rev. B* **58**, R10 091 (1998).
- <sup>10</sup>Y.-M. Lin, S. Cronin, J. Y. Ying, M. S. Dresselhaus, and J. Heremans, *Appl. Phys. Lett.* **76**, 3944 (2000).
- <sup>11</sup>J. Heremans and C. M. Thrush, *Phys. Rev. B* **59**, 12 579 (1999).
- <sup>12</sup>A. A. Nikolaeva, P. P. Bodiul, D. V. Gitsu, and G. Para, in *Thermoelectric Materials 2000-The Next Generation Materials for Small-Scale Refrigeration and Power Generation Applications*, edited by T. M. Tritt, G. S. Nolas, G. Mahan, M. G. Kanatzidis, and D. Mandrus, MRS Symposia Proceedings No. 626 (Materials Research Society, Pittsburgh, in press).
- <sup>13</sup>J. P. Heremans, in *Thermal Conductivity 25-Thermal Expansion 13*, edited by C. Uher and D. T. Morelli (Technomic, Lancaster, PA, 2000), p. 114.
- <sup>14</sup>M. S. Dresselhaus, *J. Phys. Chem. Solids Suppl.* **32**, Suppl. 1, 3 (1971).
- <sup>15</sup>L. R. Windmiller, *Phys. Rev.* **149**, 472 (1966).
- <sup>16</sup>Y.-M. Lin, X. Sun, and M. S. Dresselhaus, *Phys. Rev. B* **62**, 4610 (2000).
- <sup>17</sup>M. S. Dresselhaus and J. G. Mavroides, *Phys. Rev. Lett.* **14**, 259 (1965).
- <sup>18</sup>N. W. Ashcroft and N. D. Mermin, *Solid State Physics* (Holt, Rinehart and Winston, New York, 1976), Chap. 16.
- <sup>19</sup>M. S. Bresler and N. A. Red'ko, *Zh. Eksp. Teor. Fiz.* **61**, 287 (1971) [*Sov. Phys. JETP* **34**, 149 (1972)].
- <sup>20</sup>G. A. Saunders and Ö. Öktü, *J. Phys. Chem. Solids* **29**, 327 (1968).
- <sup>21</sup>R. Hartman, *Phys. Rev.* **181**, 1070 (1969).
- <sup>22</sup>R. Chambers, *Proc. R. Soc. London, Ser. A* **202**, 378 (1950).
- <sup>23</sup>D. E. Beutler and N. Giordano, *Phys. Rev. B* **38**, 8 (1989).